

12. T. W. Ebbesen *et al.*, *Chem. Phys. Lett.* **209**, 83 (1993).
13. N. Hamada, S. Sawada, A. Oshiyama, *Phys. Rev. Lett.* **68**, 1579 (1992).
14. R. Saito, M. Fujita, G. Dresselhaus, M. S. Dresselhaus, *Appl. Phys. Lett.* **60**, 2204 (1992).
15. J. W. Mintmire, B. I. Dunlap, C. T. White, *Phys. Rev. Lett.* **68**, 631 (1992).
16. X. Blase, L. X. Benedict, E. L. Shirley, S. G. Louie, *ibid.* **72**, 1878 (1994).

17. S. Seraphin, D. Zhou, J. Jiao, J. C. Withers, R. Loutfy, *Nature* **362**, 503 (1993).
18. S. Subramoney *et al.*, *Carbon* **32**, 509 (1994).
19. Y. Saito *et al.*, *J. Phys. Chem. Solids* **54**, 1849 (1993).
20. P. M. Ajayan *et al.*, *Phys. Rev. Lett.* **72**, 1722 (1994).
21. *Handbook of Physics and Chemistry* (CRC Press, Boca Raton, FL, ed. 69, 1988).

13 June 1994; accepted 29 July 1994

## Two Identical Noninteracting Sites in an Ion Channel Revealed by Proton Transfer

Michael J. Root and Roderick MacKinnon

The functional consequences of single proton transfers occurring in the pore of a cyclic nucleotide-gated channel were observed with patch recording techniques. These results led to three conclusions about the chemical nature of ion binding sites in the conduction pathway: The channel contains two identical titratable sites, even though there are more than two (probably four) identical subunits; the sites are formed by glutamate residues that have a  $pK_a$  (where  $K_a$  is the acid constant) of 7.6; and protonation of one site does not perturb the  $pK_a$  of the other. These properties point to an unusual arrangement of carboxyl side-chain residues in the pore of a cation channel.

One of the major goals of mechanistic ion channel studies is to understand the nature of ion coordination sites in the pore that allow selective ion permeation. Recent progress has been made in the identification of amino acids that are responsible for ion binding in cyclic nucleotide-gated (CNG) channels and in voltage-dependent  $Ca^{2+}$  channels. CNG channels and voltage-dependent  $Ca^{2+}$  channels are only distantly related in their primary sequences, but their ion conduction properties are very similar. Most notably, both channel types contain high-affinity, divalent cation-binding sites that are important for channel function under physiological conditions (1, 2). In the case of  $Ca^{2+}$  channels, divalent cation-binding sites allow the channel to exclude monovalent cations and conduct only  $Ca^{2+}$ . In CNG channels, which are responsible for the initial electrical signals underlying visual and sensory transduction, binding of  $Mg^{2+}$  or  $Ca^{2+}$  in the pore reduces the effective, single-channel conductance. In photoreceptor cells, a small single-channel conductance ensures a smoothly graded electrical response to varying light intensity (2). In addition, the ability of  $Ca^{2+}$  to pass through CNG channels may also play a role in visual and olfactory sensory transduction (2, 3).

A similar amino acid composition in the pore-forming region (P-region) underlies the shared open-channel properties of CNG channels and  $Ca^{2+}$  channels (4). In both, divalent cation binding is mediated by a set of P-region Glu residues. Four Glu

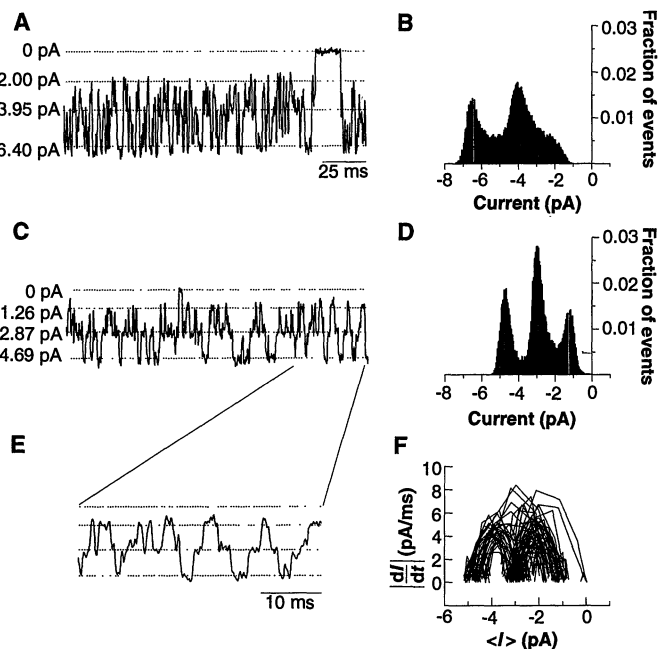
residues, one from each of the homologous domains of  $Ca^{2+}$  channels, apparently form a cluster of carboxyl groups that is capable of binding at least one (perhaps two) divalent cations (5). In an analogous fashion, a Glu residue is provided by each of the identical subunits of a CNG channel to form a divalent cation-binding site in that channel (6). To further probe the chemical groups within the pore of the CNG chan-

nel, we studied the effect of protons on ionic conduction. Our findings lead us to conclude that the P-region Glu residues are arranged so as to give rise to two identical proton-binding sites within the pore.

Experiments were done on the cloned CNG channel from catfish olfactory epithelium, expressed in *Xenopus* oocytes (7). A single channel recorded in 130 mM NaCl solution (pH 7.6, at  $-80$  mV) is shown in Fig. 1A. The open channel showed multiple poorly resolved levels of conductance; at least three are apparent in the amplitude histogram (Fig. 1B). A similar measurement made in solutions prepared with  $^2H_2O$  (deuterium oxide) is shown in Fig. 1C. Transitions between conductance levels occur at a slower rate as a result of a kinetic isotope effect (8). Under this condition, the amplitude histogram showed three distinct peaks defining the high, middle, and low conductance states (Fig. 1D). All further experiments were carried out in solutions prepared with  $^2H_2O$  to allow a detailed study of these three states.

A closer look at the current record reveals a precise connectivity among the three states. The expanded trace in Fig. 1E shows that most transitions connecting the high and low states pause for a measurable time at the middle state. The sequential connectivity is also reflected in the transient-mean analysis (Fig. 1F). Transitions appear as trajectories connecting the current levels (9). The double-arched appearance of the plot reflects a high density of trajectories connecting the middle state

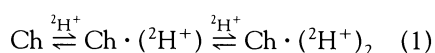
**Fig. 1.** Fluctuations of current through single olfactory CNG channels (21). (A and C) Currents were measured at a membrane potential of  $-80$  mV with 130 mM NaCl on both sides of the membrane (22). Solutions were prepared with  $H_2O$  (A) and  $^2H_2O$  (C) titrated to a pH of 7.6. The closed-state current is designated by the 0 pA line. (B and D) Open-state amplitude histograms of the channels in (A) and (C), respectively. The bin width is 0.049 pA (twice the resolution of the analog-digital converter), and the bins were normalized by the total number of measured points [39196 for (B) and 33792 for (D)]. (E) Part of the trace in (C) has been expanded to reveal the transitions between extreme conductance states. (F) For a three-point window moving along the trace in (C), the absolute value of the time derivative is plotted as a function of the mean current. Transitions between current levels in the time trace become parabolic trajectories in this transient-mean analysis (9).



Department of Neurobiology and the Biophysics Program, Harvard Medical School, Boston, MA 02115, USA.

with both the low and high states. The very low density of points connecting the two extreme states indicates that these transitions occur infrequently. Occasional direct transitions between the extremes can be accounted for by the limited time resolution of the recordings. We therefore conclude that transitions occur only between adjacent states.

The kinetic isotope effect and sequential connectivity imply that we are looking at the protonation of two separate sites on the channel. We therefore studied the effect of pH on single-channel behavior (10). At pH 9.0, the channel is most likely to be in the high conductance state, whereas at pH 6.0, the channel is almost exclusively in the low conductance state (Fig. 2A). The amplitude histograms show a gradual shift in equilibrium as pH is changed. On the basis of these results, we postulate the following sequential reaction scheme:



where Ch,  $\text{Ch} \cdot ({}^2\text{H}^+)$ , and  $\text{Ch} \cdot ({}^2\text{H}^+)_2$  represent the high, middle, and low conductance states, respectively. To quantify the equilibrium among the three states, nor-

malized amplitude histograms were fit with a sum of three Gaussian functions (Fig. 2B). The equilibrium probability of a state corresponds to the relative area under its curve. The pH dependences of these relative areas (Fig. 2C) correspond to the simplest imaginable case of scheme 1: The two protonatable sites are equivalent and independent of one another. Equivalence implies that the two sites have the same  $pK_a$  and that protonation of either site has the same effect on ion conduction. Independence means that titration of one site is not influenced by the protonation state of the other. The probability that one of these sites is protonated is given by

$$\rho = \frac{[{}^2\text{H}^+]}{[{}^2\text{H}^+] + K_a} \quad (2)$$

and the equilibrium probability of each conductance state is binomially distributed as follows:

$$P[\text{Ch}] = (1 - \rho)^2 \quad (3)$$

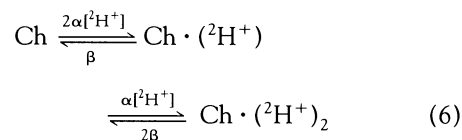
$$P[\text{Ch} \cdot ({}^2\text{H}^+)] = 2\rho(1 - \rho) \quad (4)$$

$$P[\text{Ch} \cdot ({}^2\text{H}^+)_2] = \rho^2 \quad (5)$$

This set of equations has a single adjustable

parameter,  $K_a$ . The least-squares fit (Fig. 2C) yields a  $pK_a$  of 7.6.

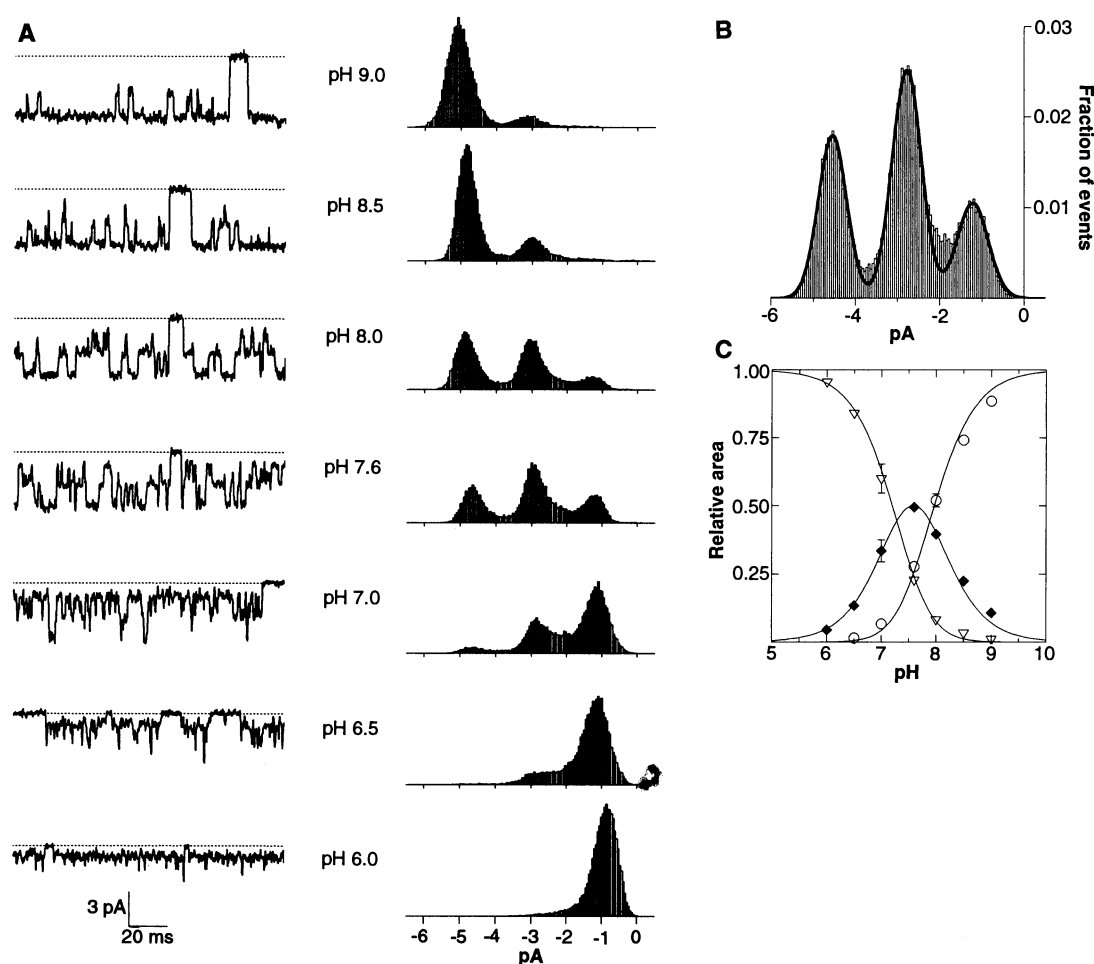
This simple model makes three strong predictions about the kinetics of protonation and deprotonation as summarized by the following scheme:



where  $\alpha$  and  $\beta$  are the rate constants for protonation and deprotonation of a single site. These three predictions are: (i) The exit rate from the high and middle conductance states should depend linearly on  ${}^2\text{H}^+$  concentration, whereas exit from the low state should be independent. (ii) The exit rate from the high conductance state should have twice the  ${}^2\text{H}^+$  concentration dependence of the exit rate from the middle state. (iii) At low  ${}^2\text{H}^+$  concentrations, the exit rate from the middle conductance state should approach half the exit rate from the low conductance state.

To test these kinetic predictions, dwell times of each conductance state were measured at different  ${}^2\text{H}^+$  concentrations, and

**Fig. 2.** The effect of pH on the conductance levels. **(A)** Single-channel currents were measured at a membrane potential of  $-80$  mV in  ${}^2\text{H}_2\text{O}$  solutions titrated to the indicated pH. The dotted line identifies the closed-state current level. The corresponding open-state amplitude histograms were constructed from many such sweeps and normalized by the total number of collected points. **(B)** An open-state amplitude histogram (pH 7.6) was fit by eye to the sum of three Gaussian functions (thick line). The area between conductance states that falls above the solid line arises from sampling transition points and accounts for less than 5% of the total area of the histogram. **(C)** The relative areas of the Gaussian functions for the low (triangles), middle (diamonds), and high (circles) conductance states are plotted against pH. The points and error bars represent the mean  $\pm$  SEM (or range of mean) of two to seven separate experiments. The solid lines through the data represent fits to a model of two equivalent and independent sites (Eqs. 2 through 5 in text) with a  $pK_a$  value of 7.58.



the resulting distributions were well approximated by single exponential functions (Fig. 3, A and B). The reciprocal time constant, or exit rate, was plotted as a function of  $^2\text{H}^+$  concentration for each state (Fig. 3, C through E). The exit rates from the high and middle states are nearly linearly dependent on  $^2\text{H}^+$  concentration and, as predicted, the slopes differ by a factor of about 2. In Fig. 3D, the  $y$  intercept ( $\beta$ ) has a value of  $0.6 \text{ ms}^{-1}$ , which is roughly half the value of the rate of exit from the low conductance state.

In two respects, scheme 6 fails to accurately account for the data. First, the exit rate from the low conductance state is affected by the  $^2\text{H}^+$  concentration (Fig. 3E). Second, a linear fit to the exit rates from the high state would not have a zero intercept (Fig. 3C). However, these deviations can be understood if we consider the transfer of  $^2\text{H}^+$  between the buffer molecule Hepes and the sites on the channel (11). Exit rates from the high conductance state are plotted as a function of total Hepes concentration at fixed pH values of 8.0, 7.6, and 7.0 (Fig. 4A). As Hepes concentration is raised, the exit rate increases, an effect that is more pronounced at low pH. This behavior is expected if the acid form of Hepes can donate a  $^2\text{H}^+$  to the site. In that case, the overall single-site protonation rate would be given by

$$\alpha[{}^2\text{H}^+] + \alpha'\Theta[\text{Hepes}]_0 \quad (7)$$

where  $\alpha$  is the second-order on-rate constant for free  $^2\text{H}^+$ ,  $\alpha'$  is the transfer rate constant from Hepes, and  $\Theta$  is the fraction of protonated Hepes [equal to  $[{}^2\text{H}^+]/([{}^2\text{H}^+] + K_{\text{aB}})$ , where  $K_{\text{aB}}$  is the acid constant of the buffer (12)]. The analogous expression for the rate of deprotonation from the low state would be given by

$$\beta + \beta'(1 - \Theta)[\text{Hepes}]_0 \quad (8)$$

where  $\beta$  is the intrinsic off-rate constant (to  $^2\text{H}_2\text{O}$ ) and  $\beta'$  is the off-rate constant for transfer to the basic form of a Hepes molecule. In agreement with Eq. 8, the exit rate from the low conductance state increases with increasing Hepes concentration, and the dependence is greater at high pH (Fig. 4B). The rate constants are estimated to be  $\alpha = 6.4 \times 10^9 \text{ M}^{-1} \text{ sec}^{-1}$ ,  $\alpha' = 5.8 \times 10^4 \text{ M}^{-1} \text{ sec}^{-1}$ ,  $\beta = 473 \text{ sec}^{-1}$ , and  $\beta' = 7.1 \times 10^4 \text{ M}^{-1} \text{ sec}^{-1}$  (13). The curves in Fig. 3, C through E, were generated by substituting Eqs. 7 and 8 for  $\alpha[{}^2\text{H}^+]$  and  $\beta$  in scheme 6. The deviations in Fig. 3, C through E from the predictions of the simple model can therefore be explained on the basis of  $^2\text{H}^+$  transfer between the sites and the buffer molecule.

In all experiments in this study, pH was adjusted on both sides of the membrane simultaneously. However, the degree of pro-

tonation is governed by the extracellular, not the intracellular, pH. This result led us to focus on externally located residues as candidates for forming the titratable sites. The P-region Glu residues are known to form a divalent cation-binding site near the extracellular side (6). The same residues also account for the conductance states induced by protonation (Fig. 5). When Glu<sup>333</sup> is replaced with Gly, the channel no longer exhibits pH-dependent subconductance levels (Fig. 5A). Interestingly, the current-voltage (i-V) relation of the mutant channel is curved like that of the low conductance state in the wild-type channel (Fig. 5B). Therefore, neutralization by ei-

ther mutagenesis or protonation seems to have the same effect on ion conduction through the channel.

When the Glu residue is replaced with an Asp, the channel shows pH-dependent fluctuations as reflected in the open channel noise (Fig. 5, C and D). However, the titration occurs over a significantly lower pH range. As a result of the reduced  $^2\text{H}^+$  affinity, discrete conductance levels are not completely resolved.

In this study, we demonstrated three unexpected properties of proton interaction with the pore of the channel. First, two equivalent protonatable sites were observed, even though the channel is com-

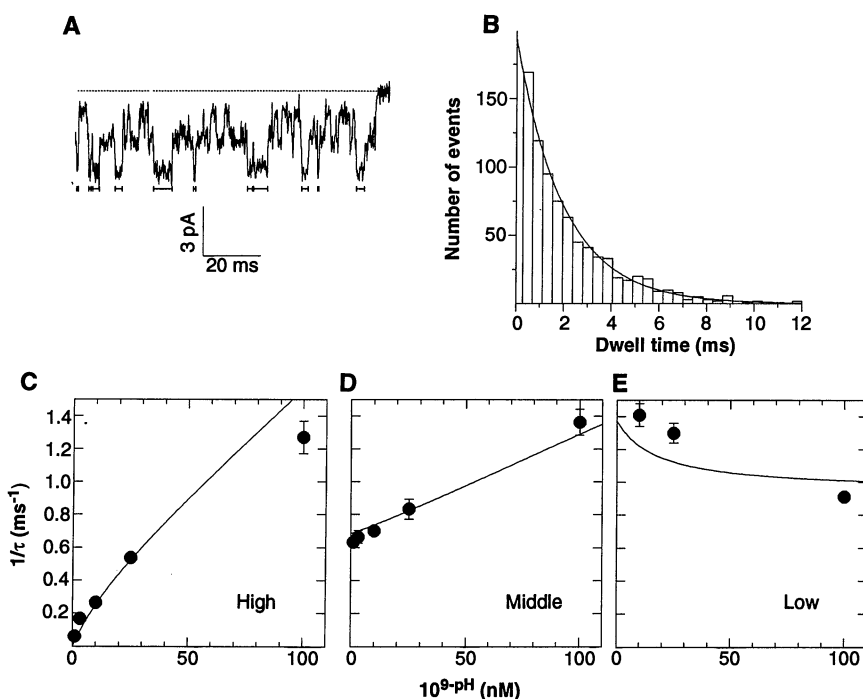
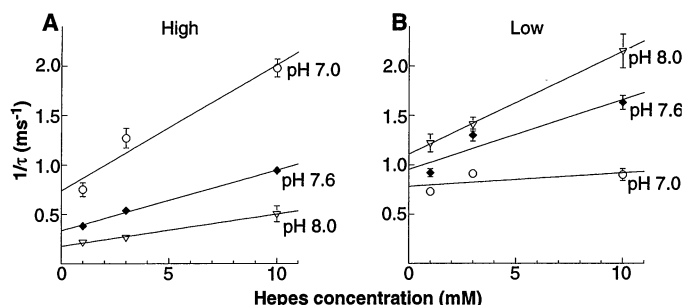


**Fig. 3.** Kinetic analysis of the transitions between current levels. (A) For a single-channel current trace ( $-80 \text{ mV}$ , filtered at  $2 \text{ kHz}$ ) in  $^2\text{H}_2\text{O}$  solutions at a pH of 7.6, the dwell times in the high conductance state are marked. Transitions between the three conductance states were determined with a manual 50% threshold criterion and cutoff times of  $0.28 \text{ msec}$  for  $2\text{-kHz}$  data and  $0.56 \text{ msec}$  for  $1\text{-kHz}$  data (1.65 times the filter rise time) (23). (B) The dwell time histogram of the high conductance state for the recording in (A) is shown. The solid line is a single exponential probability density function with a time constant equal to the arithmetic mean of the dwell times minus the cutoff time ( $0.28 \text{ msec}$ ). (C through E) The reciprocal of these calculated time constants (mean  $\pm$  SEM for three to six experiments) are plotted against  $^2\text{H}^+$  concentration for the high (C), middle (D), and low (E) conductance states. The solid curves represent an independent-equivalent two-site model that includes buffer participation in the  $^2\text{H}^+$  transfer (Eqs. 7 and 8 in text).

**Fig. 4.** The effect of buffer concentration on the rates of  $^2\text{H}^+$  transfer. The exit rates from the high (A) and low (B) conductance states are plotted against Hepes concentration for three pH values: 8.0 (triangles), 7.6 (diamonds), and 7.0 (circles). The solid lines are linear regressions.



posed of more than two (probably four) identical subunits. Second, each of the two sites formed by Glu carboxyl groups had an anomalous  $pK_a$  of 7.6. Third, protonation of one site was unaffected by the protonated state of the other. In summary, the equilibrium and kinetic description of protons interacting with the channel predict the presence of two identical and independent sites in the pore.

A free glutamic acid side-chain carboxyl has a  $pK_a$  of 4.3, but the sites in the channel titrate with a  $pK_a$  of 7.6. In proteins, Glu and Asp carboxyl groups have been found with a  $pK_a$  as high as 8.0 (14). In fact, the physical picture of several carboxyl groups in a confined pore provides a straightforward explanation for strong  $pK_a$  perturbation: Through superposition of electric fields, a charged residue will perturb the  $pK_a$  of a nearby residue. But this explanation does not adequately account for the  $pK_a$  of sites in the CNG channel because of their independent behavior—the two sites do not experience each other's electric field. This independence is highly unexpected and implies that a more subtle mechanism, perhaps one related to the precise arrangement of carboxyl side chains in the pore, must contribute to the anomalous  $pK_a$ .

Independent titration of two sites is difficult to explain in terms of the standard view of electrostatic interactions in the

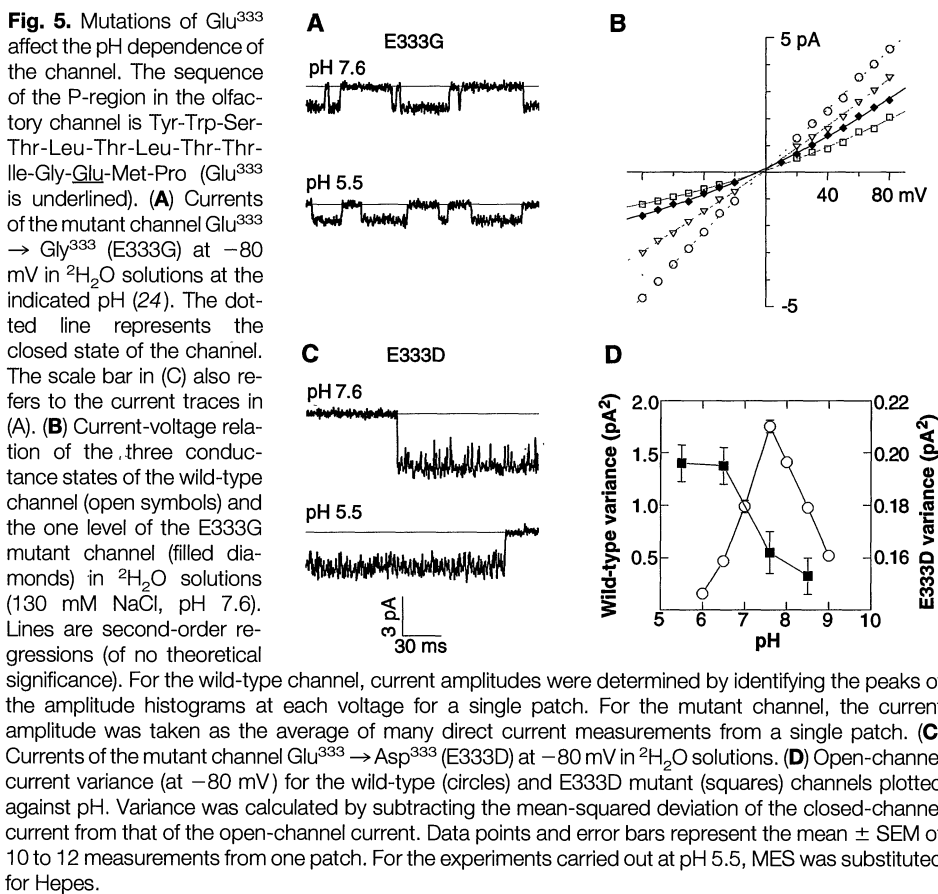
pore of an ion channel. In a confined pore, our intuition tells us that electrostatic forces should be strong. How then can two sites be independent? The difficulty here is best demonstrated through a simple calculation. From the analysis of Fig. 2, we would be able to detect a perturbation of one site by the other as small as 0.2 pH units. Using Coulomb's law and assuming an isotropic dielectric environment of 80, 0.2 pH units would require a 15 Å separation between the sites. If the effective dielectric constant is lower, then the sites would have to be even further apart. But studies on the interaction of the Glu residues with permeant blockers  $Ca^{2+}$  and  $Mg^{2+}$  place the carboxyl groups along the ion conduction pathway and therefore in close proximity.

The absence of interactions between the two sites, so strongly supported by the data, can be explained if the sites are nearly always associated with a counterion. If at any moment there is either an alkali metal cation or a proton bound, then the sites will be relatively insulated from each other. A similar concept underlies single-vacancy and ion exchange conduction mechanisms (15). A  $Na^+$  ion would only be loosely associated with a site as the ion diffuses rapidly through the pore, but a proton would dwell for a longer period of time and be detectable on the single-channel record as a change in the  $Na^+$  conduction rate.

How can one account for the presence of only two protonatable sites? If the channel has four identical subunits surrounding a central pore, then the four Glu side chains must be arranged in a precise way to form only two sites. Breakdown of the anticipated fourfold symmetry could come about in several different ways. For example, two Glu side chains might point into the pore whereas the other two point away. A second possibility is that four Glu residues could form two carboxyl-carboxylate pairs (16). A carboxyl-carboxylate consists of two carboxylate groups sharing a single proton. The unit carries a charge of minus one. Carboxyl-carboxylates occur in proteins, generally at subunit interfaces or where distant segments of a polypeptide chain come in contact (17, 18). Although pH titration data for carboxyl-carboxylates is limited, they can have an anomalously high  $pK_a$  (16, 17, 19). Because the formation of a carboxyl-carboxylate should be sensitive to side-chain length, this possibility would naturally account for the very different titration behavior of the wild-type and Asp mutant channels.

As a working model, we propose that the CNG channel has two identical, diagonally opposed sites in its pore. This twofold symmetric arrangement provides a structural basis for the functional equivalence of the sites. We further propose that these sites are located near the extracellular entryway, as they are affected by extracellular protons. These sites can be occupied by metal cations or protons. When they are protonated, or removed through mutagenesis,  $Na^+$  ions still permeate, albeit at a slower rate. The *i-v* relations shown in Fig. 5B are consistent with this picture. Removal of  $Na^+$  binding sites near the extracellular entryway induces an upward curvature accounted for by a reduced  $Na^+$  entry rate from the extracellular solution.

Discrete proton-mediated conductance levels, with properties similar to those described here, also occur in  $Ca^{2+}$  channels conducting monovalent cations (20). The  $Ca^{2+}$  channel displays only a single proton-induced subconductance level, rather than two, which indicates the presence of only a single protonatable site. This difference may be related to the fact that  $Ca^{2+}$  channels contain nonidentical domains. A conformational change has been proposed to account for the reduced conductance in the protonated  $Ca^{2+}$  channel, because the rates deviate from a simple bimolecular scheme. However, we show here that the deviations can be accounted for by proton transfer from a buffer molecule. In both channels, the mechanism underlying the subconductance levels is undoubtedly the same. We predict that Glu residues in  $Ca^{2+}$  chan-



nels, in a manner analogous to those in CNG channels, will be responsible for their proton sensitivity.

## REFERENCES AND NOTES

1. R. W. Tsien, P. Hess, E. W. McCleskey, R. L. Rosenberg, *Annu. Rev. Biophys. Biophys. Chem.* **16**, 265 (1987); G. Colamartino, A. Menini, V. Torre, *J. Physiol.* **440**, 189 (1991); F. Zufall and S. Firestein, *J. Neurophysiol.* **69**, 1758 (1993).
2. K.-W. Yau and D. A. Baylor, *Annu. Rev. Neurosci.* **12**, 289 (1989).
3. U. B. Kaupp and K.-W. Koch, *Annu. Rev. Physiol.* **54**, 153 (1991); R. H. Kramer and S. A. Siegelbaum, *Neuron* **9**, 897 (1992); T.-Y. Chen and K.-W. Yau, *Nature* **368**, 545 (1994).
4. L. Hegginbotham, T. Abramson, R. MacKinnon, *Science* **258**, 1152 (1992).
5. M.-S. Kim, T. Morii, L.-X. Sun, K. Imoto, Y. Mori, *FEBS Lett.* **318**, 145 (1993); G. Mikala, A. Bahinski, A. Yatani, S. Tang, A. Schwartz, *ibid.* **335**, 265 (1993); J. Yang, P. T. Ellinor, W. A. Sather, J.-F. Zhang, R. W. Tsien, *Nature* **366**, 158 (1993).
6. M. J. Root and R. MacKinnon, *Neuron* **11**, 459 (1993); E. Eismann, F. Muller, S. H. Heinemann, U. B. Kaupp, *Proc. Natl. Acad. Sci. U.S.A.* **91**, 1109 (1994).
7. E. H. Gouling *et al.*, *Neuron* **8**, 45 (1992).
8. W. P. Jencks, *Catalysis in Chemistry and Enzymology* (Dover, New York, 1987).
9. S. D. Tyerman, B. R. Terry, G. P. Findlay, *Biophys. J.* **61**, 736 (1992).
10. In this paper, we cite the directly measured pH; for pure  $^2\text{H}_2\text{O}$  solutions, this value is an overestimate of the actual free  $^2\text{H}^+$  concentration [L. Pentz and E. R. Thornton, *J. Am. Chem. Soc.* **86**, 6931 (1967)]. The actual value of  $-\log[^2\text{H}^+]$  can be estimated by adding 0.4 units to the cited pH.
11. The transfer could be direct or be mediated by one or more  $\text{H}_2\text{O}$  molecules between the  $\text{H}^+$  donor and acceptor [R. P. Bell, *The Proton in Chemistry* (Cornell Univ. Press, Ithaca, NY, ed. 2, 1973); E. Caldin and V. Gold, Eds., *Proton Transfer Reactions* (Wiley, New York, 1975)].
12. The measured  $\text{pK}_{\text{AB}}$  of Hepes in  $^2\text{H}_2\text{O}$  solutions is 7.74. It was determined by titration of a 30 mM Hepes solution with NaOH.
13. Microscopic reversibility would require that  $\alpha\beta'K_{\text{AB}} = \alpha'\beta$ . The rate constant magnitudes indicate that the system is out of equilibrium because of a "thermodynamic force" of about  $1 k_{\text{B}}T$ , where  $k_{\text{B}}$  is the Boltzmann constant and  $T$  is absolute temperature. The observation is explicable because the membrane is held at  $-80$  mV, and some protons exit to the inside. We discuss the results as if the system is at equilibrium, because our conclusions about the channel do not depend on the equilibrium condition. There is a twofold discrepancy between the  $K_{\text{A}}$  determined from the amplitude histogram analysis and that determined from the kinetic rate constants. We attribute this discrepancy to different systematic errors in the two measurements.
14. A. Fersht, *Enzyme Structure and Mechanism* (Freeman, New York, ed. 2, 1985).
15. H. H. Kohler and K. Heckmann, *J. Theor. Biol.* **79**, 381 (1979); M. F. Schumaker and R. MacKinnon, *Biophys. J.* **58**, 975 (1990); C. M. Armstrong and J. Neyton, *Ann. N.Y. Acad. Sci.* **635**, 18 (1991).
16. L. Sawyer and M. N. G. James, *Nature* **295**, 79 (1982).
17. D. L. D. Caspar and K. Namba, *Adv. Biophys.* **26**, 157 (1990).
18. O. Herzberg and M. N. G. James, *J. Mol. Biol.* **203**, 761 (1988); A. R. Sielecki *et al.*, *ibid.* **134**, 781 (1979); S. Mangani, P. Carloni, P. Orioli, *ibid.* **223**, 573 (1992).
19. C. A. Collyer, J. M. Guss, Y. Sugimura, F. Yoshizaki, H. C. Freeman, *ibid.* **211**, 617 (1990).
20. D. Pietrobon, B. Prod'homme, P. Hess, *J. Gen. Physiol.* **94**, 1 (1989); B. Prod'homme, D. Pietrobon, P. Hess, *ibid.*, p. 23.
21. The DNA construct for the olfactory CNG channel in the high-expression pGemHE vector was kindly provided by E. Gouling and S. Siegelbaum of Columbia University (7). RNA was synthesized from Sph 1-linearized DNA (New England Biolabs) with T7 polymerase (Promega). *Xenopus* oocytes (*Xenopus* One, Ann Arbor, MI) were prepared and injected with RNA as previously described [R. MacKinnon, P. H. Reinhart, M. M. White, *Neuron* **1**, 997 (1988)]. Inside-out patches were obtained with glass electrodes (Drummond, Broomall, PA) coated with either beeswax or Sylgard and firepolished to a resistance of 1 to 5 megohm. Single-channel currents were recorded with an Axopatch 200 (Axon Instruments) amplifier. The output of the amplifier was filtered at 1 or 2 kHz (3 dB corner frequency, 4-pole Bessel) and sampled (Indec Systems, Model IDA12120) at a frequency 7.15 times greater than the filter frequency.
22. For most electrophysiological experiments, both internal (bath) and external (pipette) solutions contained 130 mM NaCl, 3 mM Hepes, and 0.5 mM  $\text{Na}_2\text{EDTA}$  dissolved in either  $\text{H}_2\text{O}$  or  $^2\text{H}_2\text{O}$  (99.9% atom D). To activate the channels, 1 mM Na $\cdot$  cyclic guanosine 3',5' monophosphate (Sigma) was added to the internal solution. The internal and external solutions were titrated to the indicated pH with NaOH or HCl. For  $^2\text{H}_2\text{O}$  solutions, the fraction of contaminating hydrogens from Hepes, NaOH, and HCl did not exceed 0.05% of the total hydrogen and deuterium. The solution pH was measured with an Orion pH meter (Model 720) with a Corning electrode (no. 476540) that was routinely calibrated with pH 4, pH 7, and pH 10  $\text{H}_2\text{O}$  buffers.
23. Our ability to measure the calculated protonation and deprotonation rates was tested by computer simulation of the open state of a single olfactory channel. Assuming scheme 6 with time constants comparable to measured values, a current template with Gaussian noise was generated, digitally filtered, and sampled, and then run through the same analysis programs. The simulation results showed that the time resolution of the recording system was sufficient to give the values of the rates reported here. Missed events and noise do cause minor deviations in the simulated rates; these deviations are qualitatively similar to deviations of the real data from the theoretical curves in Fig. 3, C through E.
24. Cassette mutants of the pore (Mlu I-Cla I) were generated by means of polymerase chain reaction (Eri-comp; Perkin Elmer reagents) and were subcloned into the channel DNA. Mutations were confirmed by dideoxy sequencing between the restriction sites [F. Sanger, S. Nicklen, A. R. Coulson, *Proc. Natl. Acad. Sci. U.S.A.* **74**, 5463 (1977)].
25. We thank W. P. Jencks, J. Hogle, and P. Chen for helpful discussions and B. Bean, A. Gross, and L. Hegginbotham for critical review of the manuscript. Supported by NIH research grant GM47400. M.J.R. was supported by NRSA Molecular Biophysics Training Grant 5 T32 GM083113.

14 April 1994; accepted 3 August 1994

## RPS2 of *Arabidopsis thaliana*: A Leucine-Rich Repeat Class of Plant Disease Resistance Genes

Andrew F. Bent,\* Barbara N. Kunkel,† Douglas Dahlbeck, Kit L. Brown,‡ Renate Schmidt, Jerome Giraudat, Jeffrey Leung, Brian J. Staskawicz§

Plant disease resistance genes function in highly specific pathogen recognition pathways. *RPS2* is a resistance gene of *Arabidopsis thaliana* that confers resistance against *Pseudomonas syringae* bacteria that express avirulence gene *avrRpt2*. *RPS2* was isolated by the use of a positional cloning strategy. The derived amino acid sequence of *RPS2* contains leucine-rich repeat, membrane-spanning, leucine zipper, and P loop domains. The function of the *RPS2* gene product in defense signal transduction is postulated to involve nucleotide triphosphate binding and protein-protein interactions and may also involve the reception of an elicitor produced by the avirulent pathogen.

Disease resistance genes control recognition of invading pathogens and subsequent activation of defense responses (1, 2). Individual resistance genes are highly specific in function, being effective only against particular strains of a viral, bacterial, fungal, or nematode pathogen. For more than 80 years, crop breeding programs have used disease resistance genes because of their

effectiveness in preventing disease and their ease of handling as single Mendelian loci. However, the molecular basis for resistance gene function is only starting to be elucidated.

Many plant pathogens produce specific elicitor compounds that are recognized by resistant plants, thereby triggering active defense responses that curtail pathogen growth (1-3). The pathogen genes that control production of these elicitors are known as avirulence genes, and the activity of a plant resistance gene is dependent on the presence of the specific, corresponding avirulence gene in the pathogen. Defense responses observed in infected tissue include production of antimicrobial compounds and cell wall-reinforcing proteins and a localized cell death response known as the hypersensitive response (4). The physiological mechanism by which these processes are activated is not clear, al-

A. F. Bent, B. N. Kunkel, D. Dahlbeck, K. L. Brown, B. J. Staskawicz, Department of Plant Biology, University of California, Berkeley, CA 94720, USA.

R. Schmidt, Cambridge Laboratory, John Innes Centre, Norwich NR4 7UJ, UK.

J. Giraudat and J. Leung, Institut des Sciences Végétales, Centre National de la Recherche Scientifique, 91198 Gif-sur-Yvette, France.

\*Present address: Department of Agronomy, University of Illinois, Urbana, IL 61801, USA.

†Present address: Department of Biology, Washington University, St. Louis, MO 63130, USA.

‡Present address: Department of Microbiology, University of Washington, Seattle, WA 98195, USA.

§To whom correspondence should be addressed.